JOURNAL of the MEXICAN CHEMICAL SOCIETY

https://www.jmcs.org.mx/

Article

Open Access

J. Mex. Chem. Soc. **2026**, *70(1):e2456*

Received March 11th, 2025
Accepted June 11th, 2025

http://dx.doi.org/10.29356/jmcs.v70i1.2456
e-location ID: 2456

Keywords:
Carbonaceous materials, structural parameters, binary metal oxide fibers, rechargeable batteries, energy storage

Palabras clave:
Materiales carbonosos, parámetros estructurales, fibras binarias de óxido metálico, baterías recargables, almacenamiento de energía

***Corresponding author:**
Fatma Sarf
email: ftm_ozutokk@hotmail.com
Phone: +90 2862180018

ISSN-e 2594-0317

Binder-Free Lignite-Derived Carbon/$NiFe_2O_4$ Fiber Structures as a Potential Anode Material for Na-ion Batteries

Fatma Sarf[1]*, Emin Yakar[2]

[1]Çan Vocational School, Çanakkale Onsekiz Mart University, Çanakkale, Turkey.
[2]Materials Science and Engineering, Çanakkale Onsekiz Mart University, Çanakkale, Turkey.

Abstract. Rational structural design is crucial for achieving superior sodium storage performance in anode materials for Na-ion batteries. Although cost-effective coal-based carbon materials are highly attractive, their diverse structures often lead to poor performance during the Na/Na^+ process. In this study, lignite-based activated carbon/$NiFe_2O_4$ nanofiber composites were synthesized using a simple low-temperature co-precipitation method at 100 °C. $ZnCl_2$ and KOH were selected as activating agents for fabricating activated carbons from raw lignite sources. By employing different structural models, the estimated crystallite size of the lignite-based activated carbon ranges from 41 to 47 nm, while the range for $NiFe_2O_4$ nanofiber incorporation is between 95 and 143 nm. The Raman spectrum of the samples confirms sharp D, G, and shallow 2D bands of activated carbon located at ~1340, 1580, and 2700 cm^{-1}, respectively. The presence of sulfur and silicon residues in the activated carbon structure hinders sodium ion transport. The reduction of silicon content and the elimination of sulfur, combined with the incorporation of $NiFe_2O_4$ fibers and the creation of additional active zones, enhances the electrochemical performance by providing more Na-storage sites. The results indicate that the lignite-based activated carbon/$NiFe_2O_4$ nanofiber composites exhibit improved rate performance compared to individual lignite-derived activated carbons.

Resumen. El diseño estructural racional es crucial para lograr un mayor rendimiento almacenamiento de sodio en materiales para ánodos de baterías de iones de Na. Aunque los materiales de carbono a base de carbón rentables son muy atractivos, sus diversas estructuras a menudo dan como resultado un bajo rendimiento durante el proceso Na/Na^+. En este estudio, se sintetizaron compuestos de nanofibras de carbón activado/$NiFe_2O_4$ a base de lignito mediante una coprecipitación fácil a baja temperatura a 100 °C. Se seleccionaron $ZnCl_2$ y KOH como agentes activadores para la fabricación de carbones activados a partir de fuentes de lignito en bruto. Con el uso de diferentes modelos estructurales, el tamaño estimado de cristalito del carbón activado a base de lignito está entre 41-47 nm, mientras que es un rango de 95-143 nm con la incorporación de nanofibras de $NiFe_2O_4$. El espectro Raman de las muestras confirma una banda D, G nítida y 2D poco profunda de carbón activado que se ubicó en ~1340, 1580 y 2700 cm^{-1}, respectivamente. La presencia de residuos de azufre y silisio en la estructura del carbón activado dificultó el transporte de iones sodio. La reducción del contenido de silicio y la eliminación de azufre, combinada con la incorporación de fibras de $NiFe_2O_4$ y la creación de zonas más activas, mejoraron el rendimiento electroquímico al proporcionar sitios adicionales de almacenamiento de iones Na. Los resultados indican que los compuestos de nanofibras de carbón activado a base de lignito/$NiFe_2O_4$ exhiben un mejor rendimiento de velocidad en comparación con los carbones activados individuales derivados del lignito.

Introduction

Rechargeable batteries play a pivotal role in the transition from fossil fuels to renewable energy sources, as they help balance supply and demand during peak load periods. Recent sustainability-oriented research has focused on Na-ion batteries, which offer lower fabrication costs, a broader operational temperature range, reduced risk of thermal runaway, and more abundant reserves compared to Li-ion batteries [1-2]. However, challenges related to electrode active materials, such as high energy barriers for Na^+ ion diffusion (1.02 Å), low Na^+ ion mobility, low volumetric energy density, and high electrode potential, which stress the electrolyte, remain to be addressed [3]. Therefore, the design of advanced anode materials is crucial for the large-scale production and commercialization of Na-ion batteries.

In recent years, coal-based carbons have emerged as promising candidates for anode materials in Na-ion batteries due to their high Na^+ storage capacity, micro- and nano-porous structures, tunable layer spacing, negligible solid electrolyte interphase (SEI) layer formation, lower environmental impact, and cost-effectiveness compared to traditional graphite [4-5]. However, their diverse structures also present drawbacks, including low electrical conductivity, low initial Coulombic efficiency (ICE), and significant volume expansion during the sodiation-desodiation process (Na/Na^+; −2.71 V) [6-7]. Wang et al. demonstrated a reversible capacity of 300.6 mAh/g at 0.1 C for lignite-derived soft carbons across a wide temperature range (40–80 °C) [8]. To mitigate capacity retention issues, incorporating additional active sites in the anode is considered an effective strategy to improve interface compatibility and increase interlayer distance [9]. Yang et al. synthesized lignite-derived hard carbon with micron-sized carbon tubes, achieving a high reversible capacity of 244.8 mAh/g and an ICE of 76.72 % [10]. Encapsulated N, P-codoped lignite-based carbon with MnS demonstrated a capacity of 392.5 mAh/g even at 1.6 A g^{-1} [11]. High reversible capacity (282.9 mAh/g) and excellent ICE (87.1 %) were achieved by controlling low-temperature pyrolysis instead of direct carbonization of lignite-based carbons [12]. These results indicate that active sites such as interlayer spaces, defects, pores, functional groups, edges, and heteroatoms significantly influence Na-storage performance [13]. Therefore, we propose the incorporation of binary metal oxide fibers on Çan lignite-based carbon surfaces to create various active sites. The morphological robustness of $NiFe_2O_4$ nanofibers during the conversion reaction improved the specific capacity by forming a conductive network along the electrode, as demonstrated in our previous study [14]. For example, cluster-like vapor-grown carbon fiber/$NiFe_2O_4$ exhibited an initial discharge capacity of 1653 mA h g^{-1} at a current density of 100 mAg^{-1} for Li-ion batteries [15]. However, they tend to aggregate strongly, which somewhat restricts their electrochemical performance in energy storage systems [16]. The nanofiber morphology is expected to offer several advantages in battery performance compared to other morphologies, due to its higher specific surface area and aspect ratio, which effectively improve the electrolyte-ion diffusion process [17].

In this paper, we aim to investigate the relationship between the microstructure and Na-storage performance in lignite-derived carbon/$NiFe_2O_4$ fiber nanocomposites. The conversion of physical and chemical properties in activated carbons has been systematically examined by incorporating binary metal oxide fibers.

Experimental

Raw lignites (~100 mesh) were supplied from Çan Lignite Facilities, Turkey. After the grinding and screening processes, to reduce the ash content and mineral impurities of raw lignites, they were ultrasonically cleaned with $HCl:H_2O_2$/[1:1] for 3 h. After filtration and repeated washing, the cleaned lignites were carbonized to pyrolysis in a tubular furnace under the nitrogen atmosphere at 850 °C (TG-DTA curve was exhibited in Fig.1.) for 1 h with a heating rate of 10 °C/min and flow rate of 0.5 $Lmin^{-1}$. TG-DTA curves of Çan lignite was found to be compatible with the previous study [18]. One-step chemical activation process was employed, followed by the addition of a specific proportion of the activators m_{ZnCl2}/m_{KOH}= 0.50/0.96 g at 70 °C for 3 h. Activated carbons were obtained by repeating the washing with ethanol-distilled water and drying processes (80 °C for 1 h) several times. The resulting lignite-derived carbon is labeled as CL. 0.04 g $NiFe_2O_4$ nanofibers (detailed production of these fibers was explained in our previous study) were stirred CL samples in ethanol solution along 6 h at 60 °C [14]. Obtained powders filtered, dried at room temperature, and finally labeled as CLN.

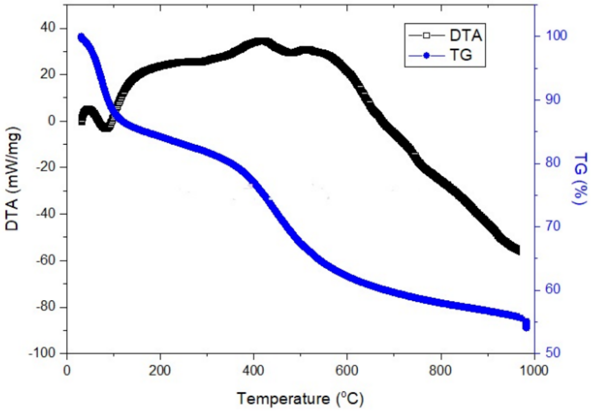

Fig.1. TG-DTA curve of raw lignite

X-ray diffraction measurements were performed using Rigaku Smart-Lab diffractometer equipped with CuK_α radiation in the 2ϴ=10°-80° range. FE-SEM images were exhibited by using JEOL-7100F microscope in connection with OXFORD Instruments X-Max energy dispersive atomic x-ray spectroscopy (EDAX). TEM measurements were conducted in an HT-7700 apparatus at 200 keV. For the TG-DTA measurements, a Shimadzu DTG-60/60H was used. The Raman spectrum of the samples was recorded using a 780 nm laser line, spanning from 4000 to 0 cm^{-1}.

The electrochemical characteristics of both materials were investigated using CR2032 half-cells. Slurries were prepared by weighing the active material and carbon super P conductive agent in an 80:20 ratio, respectively. The slurries were cast onto an Al-foil current collector and dried overnight at 70 °C in a vacuum oven. During the electrochemical tests, sodium metal (Sigma Aldrich) was used as the reference and counter electrodes. 1 M $NaPF_6$ PC solution containing a 5 wt% FEC was used as electrolyte. The capacity values were calculated based on the total mass of the active materials. Galvanostatic charge and discharge tests, with a voltage range of 0.05–3.0 V, were performed using the Neware.

Results and discussion

Structural properties

x-ray diffraction (XRD) patterns of both samples reveal a graphitic carbon structure with typical (002) and (100) peaks, assigned to JCPDS card no: 00-056-0159, as shown in Fig. 2. The samples exhibit which corresponding to (040) peak (also CL sample has S(266) peak) for S [JCPDS card no: 4-8-0247] and (100) peak for SiO_2 [JCPDS card no: 046-1015], attributed to the low carbonization temperature of 850 °C, high sulphur content (3.35 %) and high disordering degree of raw lignite, as shown in sulfur and silisium (w%) content from EDX analysis [19]. The (002) peak at ~23°, assigned to graphitic planes, shifts to a lower angle at ~22°, indicating a decrease in the stacking thickness of graphitic layers for CL and CLN samples [20]. Additionally, activation with KOH and $ZnCl_2$ generates different compounds that introduce defects into the carbon matrix, increasing the spacing between activated carbon layers [21]. The CLN samples exhibit a mixed structure of graphitic carbon and $NiFe_2O_4$, along with some residues. The characteristic cubic spinel $NiFe_2O_4$ structure is assigned to JCPDS card no: 10-0325. Interestingly, the preferential orientation of the CLN sample is the (112) peak of Fe_2O_3 ($2\theta = 26.78°$) as a component of $NiFe_2O_4$ fibers [14]. Another residue peak corresponds to NiO (111), which is assigned to JCPDS card no 47-1049. The presence of the (112) peak at 26.78° was attributed to Fe_2O_3 as a component within the $NiFe_2O_4$ spinel structure, based on prior reports of similar systems where secondary phases may arise due to localized stoichiometric variations or synthesis conditions. The unindexed peaks likely stem from minor impurities (e.g., silicates or Al compounds) inherent to the lignite source, as reflected in the EDX analysis. The Fe_2O_3-like signal in CL (without $NiFe_2O_4$) may originate from trace Fe impurities in raw lignite (0.16 wt%, Table 2), which could form oxides during carbonization.

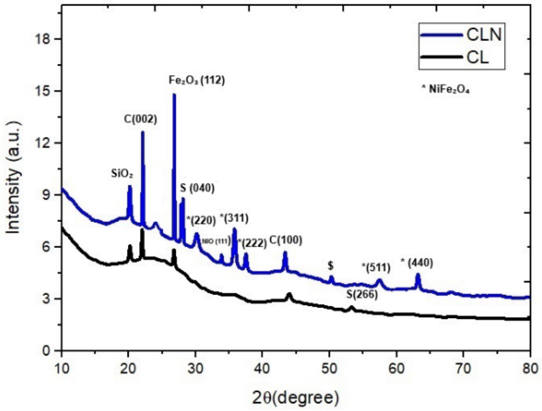

Fig.2. x-ray patterns of CL and CLN samples.

With deviation from perfect crystallinity, the nanocrystal's expansion peaks are due to size confinement, which then leads to point defects, dislocation density, triple junctions, grain boundaries, sintering stress, and internal stress caused by stacking [22]. In order to be able to discuss these effects that the traditional Debye-Scherrer model alone cannot offer, the determination of crystal size and intrinsic (micro) strain parameters using various models has been so important [23]. The estimated crystal size and intrinsic strain of CL and CLN samples were measured by Modified Scherrer (M-S), Williamson-Hall (the Uniform Deformation model, which is a part of it) (UDM), Size-Strain (S-S), and Halder-Wagner(H-W) methods and graphs and results were presented in Fig. 3 and Table 1, respectively. Many studies are using different types of nanoparticles such as Ga_2O_3, TiO_2, Ag_2O and ZnO which include the equations, advantages and challenges of these methods [22-24]. The characterization of crystal structures is truly crucial as structural defects will have significant ramifications on electrochemical properties [24]. After plotting, a straight line was generated, and by comparing the obtained straight line with the straight-line equation ($y = ax+b$), the crystallite size and strain were evaluated. According to the model type, estimated crystallite size and strain were calculated from the slope and the intercept. The minimum and maximum crystallite size is measured by using the Size-Strain and Halder-Wagner methods, respectively. The minimum and maximum intrinsic strain is measured by using Halder-Wagner and Scherrer method, respectively. In addition, the estimated crystallite size of CLN samples is double, while the strain values of CLN samples are lower compared to CL samples due to particle aggregation. This could be attributed to the inhomogeneous lattice deformations along the crystallographic activated carbon planes [25].

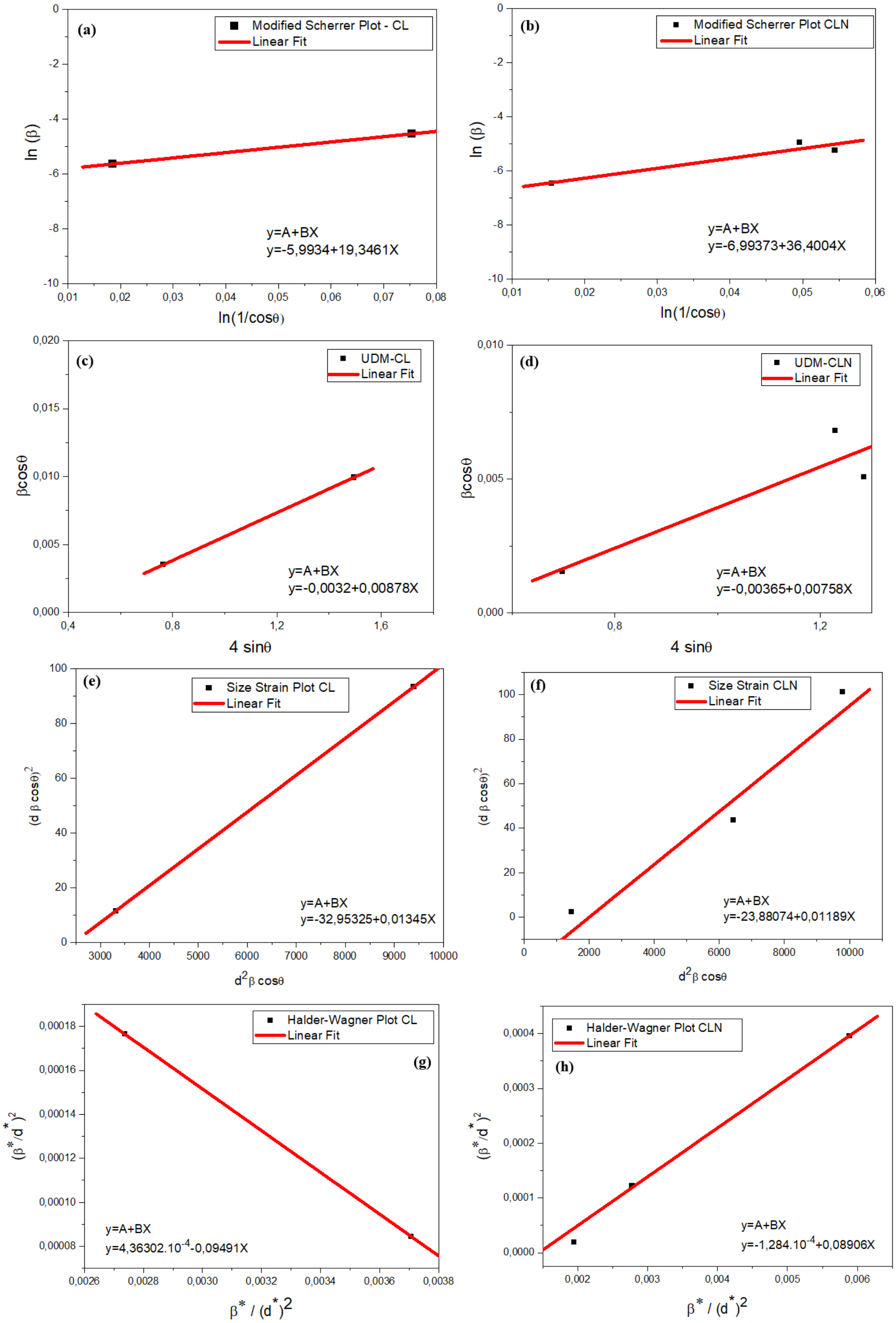

Fig.3. **(a-b)** Modified Scherrer plot, **(c-d)** Uniform Deformation plot, **(e-f)** Size-strain plot and **(g-h)** Halder-Wagner plot of CL and CLN samples.

J. Mex. Chem. Soc. **2026**, *70(1):e2456*
Regular Issue

ISSN-e 2594-0317

Table 1. Structural parameters of CL and CLN samples according to different methods

	Scherrer		**Modified Scherrer**		**Uniform Deformation**		**Size–Strain**		**Halder–Wagner**	
	D(nm)	ε (10^{-3})	D(nm)	ε (10^{-3})	D(nm)	ε(10^{-3}) tensile strain [25]	D(nm)	ε (10^{-3})	D(nm)	ε (10^{-3})
CL	41	32	43	3.2	41.5	2.7	29.5	11.3	47	1.3
CLN	95	14	66	5.2	37	2.0	34.5	9.7	143	0.7

Microstructure and elemental analysis

The microstructure of CL and CLN samples is shown in Fig. 4. and Fig. 5, using FE-SEM and TEM images. The CL sample displays an irregular, massive crystal structure with cracks and a rough surface. Particle agglomeration on the CL surface limits the nanomaterial's specific size effect by reducing intergranular space, thereby inhibiting ion transport, as seen in Fig. 4**(a)** and Fig. 4**(b)** [26]. In Fig. 4**(c)** and Fig. 4**(d)**, $NiFe_2O_4$ fibers are covered with activated carbon particles, resulting in a more regular surface. Similar surface modifications by Toghan et al. demonstrated improved specific capacity with $NiFe_2O_4$/AC composites compared to their components in supercapacitor application [27]. The $NiFe_2O_4$ fibers and activated carbons form nanocomposite fibers with a standard fiber structure, indicating that $NiFe_2O_4$ nanoparticles and activated carbons are embedded on the fiber surface through a fusion process [14]. TEM images confirm the heterogeneity of the CL sample, with distinct shapes indicating variations in the crystalline structure, as shown in Fig. 5**(a)**. The inner radius of the $NiFe_2O_4$ fiber increases from ~580 nm to ~1258 nm due to particle aggregation upon activated carbon decoration. However, some large-sized particles remain, as seen in Fig. 5**(b)** from TEM images [28]. The shape formation is due to the overlap between $NiFe_2O_4$ and activated carbon along their direction of growth [29].

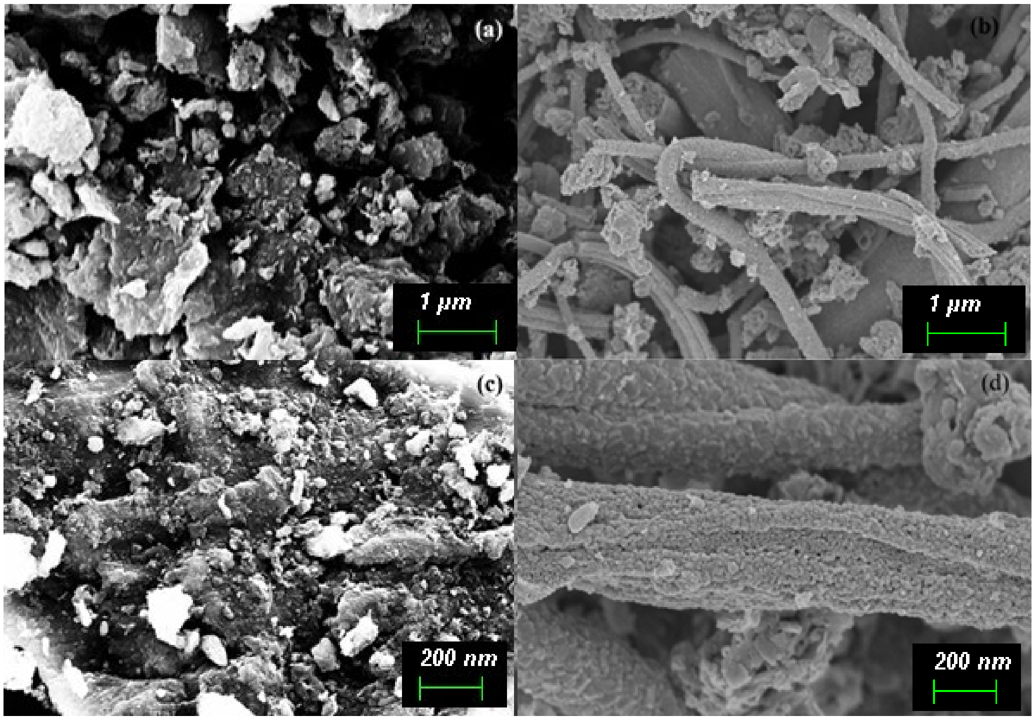

Fig.4. FE-SEM images of CL and CLN surfaces under **(a-b)** low-magnification (x5000) and **c-d)** high-magnification ratio (x30000).

http://dx.doi.org/10.29356/jmcs.v70i1.2456

J. Mex. Chem. Soc. **2026**, *70(1):e2456*
Regular Issue

ISSN-e 2594-0317

Table 2. The mass proportion of elements in CL and CLN samples.

Element	CL (Atomic Ratio) (w%)	CLN (Atomic Ratio) (w%)
C	62.96	45.25
O	16.07	43.08
Al	5.75	2.38
Si	9.90	2.73
Mn	-	0.13
Fe	0.16	3.61
Ni	-	3.28
S	1.71	-

From Table 2, both samples have a high content of C and O. The atomic ratio of Fe and Ni relatively increases in the CLN samples due to the low amount of $NiFe_2O_4$ fibers. Si restricts ion transport due to its natural insulating property, and the elemental ratio of Si decreases in CLN samples. The CL sample has Al and S residue elements. In contrast, the CLN sample has Al and Mn, indicating that the powder used in continuous casting was unintentionally introduced during the synthesis process.

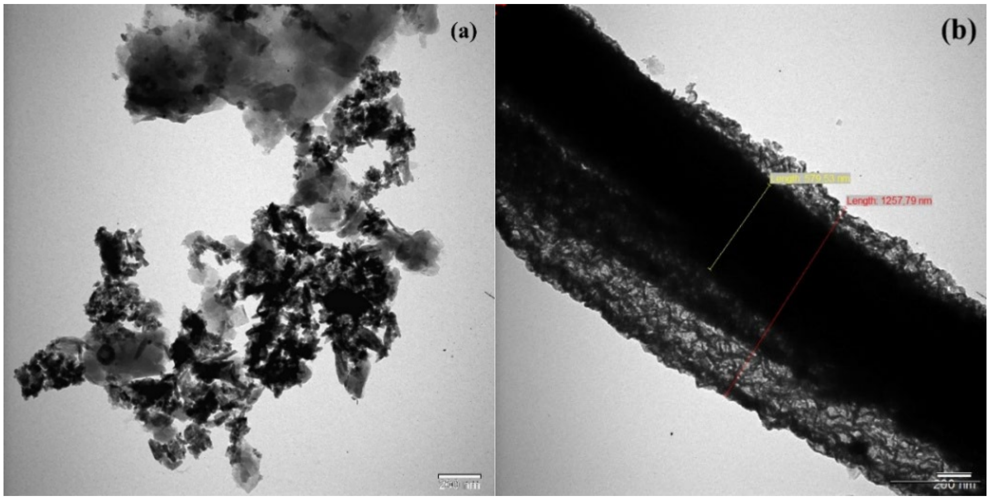

Fig. 5. TEM micrograph of CL **(a)** and CLN **(b)** samples.

http://dx.doi.org/10.29356/jmcs.v70i1.2456

Raman spectrum

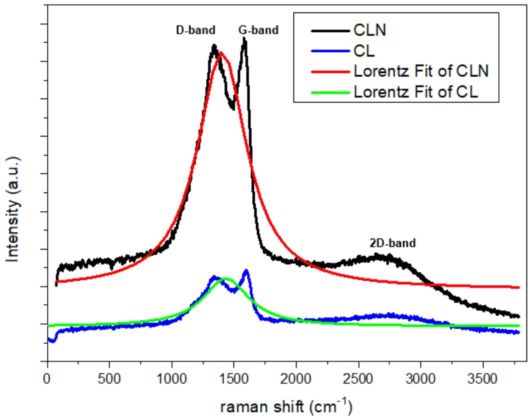

Fig. 6. Raman and deconvoluted Raman spectra of CL and CLN samples.

Table 3. Raman peak parameters of CL and CLN samples.

	D-peak position (cm^{-1})	G-peak position (cm^{-1})	D-peak width (cm^{-1})	G-peak width (cm^{-1})	I_D/I_G
CL	1340	1580	225	125	0.98
CLN	1340	1600	210	150	0.98

Raman spectra of CL and CLN samples are shown in Fig. 6. Raman spectroscopic analysis revealed distinct structural characteristics of the CL and CLN samples, as summarized in Table 3. The spectra (Fig. 6) exhibited the characteristic D (~1340 cm^{-1}) and G (~1580-1600 cm^{-1}) bands of carbonaceous materials, with no observable $NiFe_2O_4$-related phonon modes in CLN, consistent with the minimal contribution of these fibers in the 200-800 nm spectral range [30]. These spectral modifications are consistent with previous reports on defect-engineered carbon materials [31,32], where: The G-band shift reflects changes in the crystalline ordering of graphitic domains, the width variations indicate alterations in the distribution of sp^2-bonded clusters, and the preserved ID/IG ratio suggests maintained defect density despite structural reorganization. The observed 2D band (~2700 cm^{-1}) showed reduced intensity in CLN, consistent with the incorporation of $NiFe_2O_4$ fibers and consequent modification of the graphene-like layer structure [31]. These structural characteristics, particularly the increased G-band width and maintained defect density, may enhance the material's capability for Na-ion accommodation, as suggested by previous studies on disordered carbon anodes [32].

To improve the accuracy of determinations of peak position, width, or band integral intensity, a procedure for curve deconvolution has been performed, as seen in Fig.6. The G-band peak position was sensitive to the crystalline state, which was affected by the presence of defects and/or surface oxygen groups in the graphitic structure [33]. The intensity ratio ($R = I_D/I_G$) of CL and CLN samples is shown in Table 3. The spectral deconvolution procedure, as seen in Fig. 6, confirmed the reliability of the peak parameters presented in Table 3, with the G-band position and width being susceptible to the crystalline state and defect configuration of the carbon matrix [34]. In addition, the width of the G-peak is proportional to the bond angle disorder in the sp^2 regions, while an increase in the width of the G-peak indicates an increased bond angle disorder in the sp^2 distorted rings and chains for CLN. A shallow peak at ~2700 cm^{-1} corresponds to the 2D (G') band, which corresponds to the harmonic (second order Raman scattering) of an in-plane transverse optical (TO) mode close to the zone boundary K point. The intensity of this peak increases with $NiFe_2O_4$ fibers, indicating that the graphene layers are decreasing.

Electrochemical properties

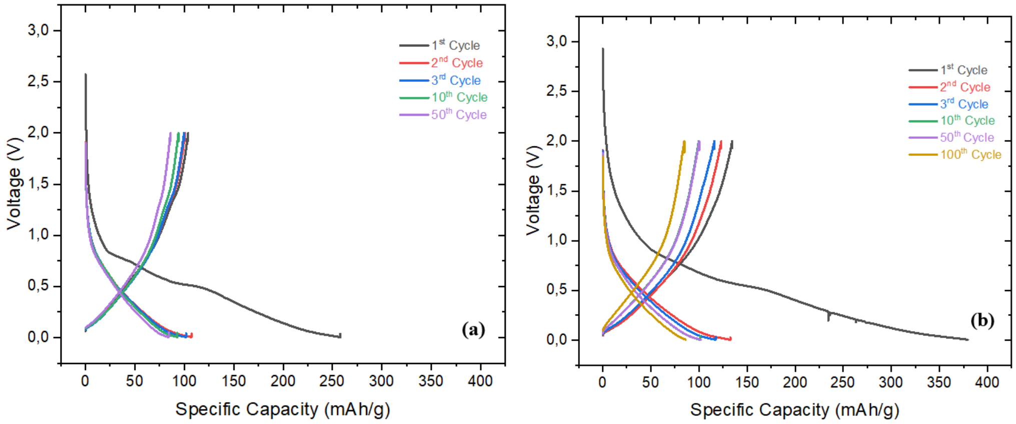

Fig.7. Galvanostatic charge/discharge profiles of sodium-ion battery half cells for **(a)** CL and **(b)** CLN anodes.

Galvanostatic charge/discharge profiles of sodium-ion battery half-cells for CL and CLN anodes are shown in Fig. 7 V with a specific voltage of 0.05–3.0 V for the sodium-ion half cell. The CL electrode operated for 50 cycles, while the CLN electrode delivered a capacity for 100 cycles, suggesting that the reduction of residues and introducing defects into the carbon matrix with $NiFe_2O_4$ fibers accelerates Na^+ diffusion and mitigates structural instability [35]. The fiber structure provides a conductive network and synergistic effects for ion penetration and transport, serving as a reservoir for Na ions [36]. In addition, $NiFe_2O_4$ undergoes reversible conversion reactions during cycling as shown in Equations 1 and 2.

$$NiFe_2O_4 + 8Na^+ + 8e^- \leftrightarrow Ni + 2Fe + 4Na_2O \qquad \text{(Equation 1)}$$

Fe_2O_3, as detected in XRD analysis in 3.1, contributes additional capacity *via*;

$$Fe_2O_3 + 6Na^+ + 6e^- \leftrightarrow 2Fe + 3Na_2O \qquad \text{(Equation 2)}$$

The CLN anode delivers a discharge capacity of 378 mAh/g and a charge capacity of 130 mAh/g due to the defects in both samples. Although capacity decay occurs over cycles for both electrodes, CLN exhibits better cycling performance due to enable better electrolyte penetration through interconnected porosity, improved cycling stability (100 vs. 50 cycles) demonstrates structural benefits and reduced polarization in charge/discharge profiles, as seen in Fig. 7, indicates enhanced kinetics [37]. Also, due to the special crystal structure of α-Fe_2O_3, which is more conducive to the transmission of Na^+ [38].

Conclusions

In this study, we investigated the structural, morphological, and electrochemical properties of lignite-based activated carbon/$NiFe_2O_4$ nanofiber composites and explored their potential as an anode in Na-ion batteries. FE-SEM and TEM images, as well as the XRD spectrum, confirmed that the samples were well indexed to the graphitic carbon crystal structure, as well as the cubic spinel $NiFe_2O_4$ structure, with some residual peaks (Si, S, NiO) present. Various structural models (M-S, W-H, S-S, H-W) were employed to compare the sample's estimated crystal size and intrinsic strain. Detailed Raman spectrum analysis has shown that the increasing crystallinity of the lignite-based activated carbon/$NiFe_2O_4$ nanofiber composites is accompanied by an increase in defects, which promotes greater Na-ion transport compared to lignite-derived activated carbons. The structural instability of lignite-derived carbon reduces sodium ion retention capacity. This study provides insights into the sodium storage mechanism in coal-based carbons and suggests the design of advanced nanofibers to enhance performance.

Acknowledgements

This study was supported by Scientific Research Unit of Çanakkale Onsekiz Mart University (project no: FBA-2019-3040). We would like to thank Rezan Demir Çakan and Edanur Aktürk for measuring the battery test conducted at Gebze Technical University.

References

1. Bartoli, M.; Piovano, A.; Elia, G.A.; Meligrana, G.; Pedraza, R. et.al. *Renew. Sustain. Energy Rev.* **2024,** *194*, 114304. DOI: https://doi.org/10.1016/j.rser.2024.114304
2. Shao, Y.; Zhang, Y.; Jiang, N.; Hao, Y.; Qu, K.; Zeng, Y.; Liu, Z.; Lu, X.; Li, Y.; Yang, Q.; Qiu, J. *iScience.* **2023**, *26*, 108470. DOI: https://doi.org/10.1016/j.isci.2023.108470
3. Yan, G.; Mariyappan, S.; Rousse, G.; Jaquet, Q.; Deschamps, M.; David, R.; Mirvaux, B.; Freeland, J.W.; Tarascon, J. *Nat. Commun.* **2019**, *10*, 585 DOI: http://dx.doi.org/10.1038/s41467-019-08460-2
4. Yang, Z.; Zhang, C.; Li, F.; Xing, B.; Zhang, Y.; Qu, X.; Yu, J.; Xu, L. J. *Energy Storage.* **2025**, *145*, 119901. DOI: http://dx.doi.org/10.1016/j.est.2025.119901
5. Ma, S.; Yan, W.; Dong, Y.; Su, Y. *Mater. Today.* **2024**, *75*, 334-358. DOI: https://doi.org/10.1016/j.mattod.2024.03.010
6. Jayamkondan, Y.; Penki, T.R.; Nayak, P.K. *Mater. Today Energy.* **2023**, *36*, 101360. DOI: https://doi.org/10.1016/j.mtener.2023.101360
7. Phogat, P.; Rawat, S.; Dey, S.; Wan, M. *J. Alloys Compd.* **2025**, *1020*, 179544. DOI: https://doi.org/10.1016/j.jallcom.2025.179544
8. Wang, R.; Fan, Y.; Wang, J.; Li, Y.; Li, X.; Jin, F.; Hu, X. *Prog. Nat. Sci.:Mater. Int.* **2024**, *34*, 1281-1294. DOI: https://doi.org/10.1016/j.pnsc.2024.11.002
9. Chen, D.Q.; Zhang, W.; Luo, K.Y. et.al. *Energy Environ. Sci.* **2021**, *14*, 2244-2262. DOI: https://doi.org/10.1039/d0ee03916k
10. Yang, Z.; Huang, T.; Liu, G.; Wei, Y.; Zhang, Y.; HXue, H.; Zhang, L. *Mater. Today Sustain.* **2024,** *27*, 100929. DOI: https://doi.org/10.1016/j.mtsust.2024.100929
11. Lan, D.; Zhao, Y.; Liu, Y.; Zhu, N.; Cui, J. *J. Energy Storage.* **2024**, *90*, 111827. DOI: https://doi.org/10.1016/j.est.2024.111827
12. Lin, Y.; Jia, J.; Wang, J.; Kang, X.; Huang, G.; Xing, B.; Kang, W.; Zhang, C. *Chem. Eng. J.* **2025**, 504, 158858. DOI: https://doi.org/10.1016/j.cej.2024.158858
13. Wang, X.; Lin, J.; Li, F.; Shen, H.; Luo, C. et.al. *J. Energy Storage.* **2025**, *112*, 115544. DOI: https://doi.org/10.1016/j.est.2025.115544
14. Sarf, F.; Eroğlu, Ö.; Kızıl, H. *Mater. Today: Proc.* **2023**, *93*, 75-78. DOI: https://doi.org/10.1016/j.matpr.2023.07.314
15. Santhoshkumar, P.; Kang, S.H.; Shaji, N.; Lee, C.W. *J. Alloys Compd.* **2020**, 842. DOI: https://doi.org/10.1016/j.jallcom.2020.155649
16. Zhang, Y.; Zhang, Y.; Li, C.; Yan, X. et.al. *Coord. Chem. Rev.* **2024**, *519*, 216103. DOI: https://doi.org/10.1016/j.ccr.2024.216103

17. Rezić Meštrović, I.; Somogyi Škoc, M. *Polymers* **2025**, *17*, 1456. DOI: http://dx.doi.org/10.3390/polym17111456
18. Oikonomopoulos, I.K.; Perraki, M.; Tougiannidis, N. et.al. *Int. J. Coal Geol.* **2013**, 115, 1-12. DOI: https://doi.org/10.1016/j.coal.2013.04.002
19. Tian, X.; Luo, S.; Wang, G.; Li, L.; Sun, M.; Wang, Q.; Li, C. *J Energy Storage*. **2025**, *113*, 115684. DOI: https://doi.org/10.1016/j.est.2025.115684
20. Lan, N.; Shen, Y.; Li, J.; Zeng, L.; Luo, D.; He, H.; Zhang, C. *J. Colloid Interface Sci.* **2024,** *675*, 293-301. DOI: https://doi.org/10.1016/j.jcis.2024.06.196
21. Feng, H.; Zhou, T.; Ge, L.; Li, Q.; Zhao, C.; Huang, J.; Wang, Y. *Energy*. **2024**, *292*, 130570. DOI: https://doi.org/10.1016/j.energy.2024.130570
22. Tamanna, N.J.; Md. Hossain, S.; Md. Bahadur, N.; Ahmed, S. *Results Chem.* **2024**, *7*, 101313. DOI: https://doi.org/10.1016/j.rechem.2024.101313
23. Nasiri, S.; Rabiei, M.; Palevicius, A.; Janusas, G.; Vilkauskas, A.; Nutalapati, V.; Monshi, A. *Nano Trends*. **2023,** *3*, 100015. DOI: https://doi.org/10.1016/j.nwnano.2023.100015
24. Lim, J.S.; Yam, F.K. *Physica B: Condensed Matter*. **2025**, *699*, 416798, https://doi.org/10.1016/j.physb.2024.416798
25. Nikmehr, S.; Md. Kazemzad, Md. Sabzehmeidani, M.; Nikzad, L.; Ebadzadeh, T. *OpenNano*. **2024**, *16*, 100203. DOI: https://doi.org/10.1016/j.onano.2024.100203
26. Jose, A.; Porel, M. *Microchem. J.* **2025**, *208*, 112596. DOI: https://doi.org/10.1016/j.microc.2024.112596
27. Toghan, A.; Khairy, M.; Kamar, E.M.; Mousa, M.A. *J. Mater. Res. Technol.* **2022**, *19*, 3521-3535. DOI: https://doi.org/10.1016/j.jmrt.2022.06.095
28. Hao, S.; Sheng, X.; Xie, F.; Sun, M.; Diao, F.; Wang, Y. *J. Energy Storage*. **2024,** *80*, 110412. DOI: https://doi.org/10.1016/j.est.2023.110412
29. Montero-Muñoz, M.; Ramos-Ibarra, J.E.; Rodríguez-Páez, J.E.; Marques G.E.; Teodoro M.D.; Coaquira J.A.H. *Phys. Chem. Chem. Phys.* **2020**, *14*, 7329-7339. DOI: https://doi.org/10.1039/c9cp06744b
30. Muhaymin, A.; Mohamed, H.E.A.; Hkiri, K.; Safdar, A.; Kotsedi, L.; Maaza, M. *Mater. Today Chem.* **2024**, *40*, 102286. DOI: https://doi.org/10.1016/j.mtchem.2024.102286
31. Baek, J.; Shin, H.; Chung, D.C.; Kim, B. *J. Ind. Eng. Chem.***2017**, *54*, 324-331. DOI: https://doi.org/10.1016/j.jiec.2017.06.007
32. Li, Y.; Ni, B.; Li, X. *Nano-Micro Lett.* **2019,** *11*, 60. DOI: https://doi.org/10.1007/s40820-019-0291-z
33. Yoshikawa, Y.; Teshima, K.; Futamura, R.; Tanaka, H.; Neimark, A.V.; Kaneko, K. *J. Colloid Interface Sci.* **2020**, *578*, 422-430. DOI: https://doi.org/10.1016/j.jcis.2020.06.002
34. Cançado, L.G.; Monken, V.P.; Campos, J.L.E.; Santos, J.C.C.; Backes, C.; Chacham, H.; Neves, B.R.A.; Jorio, A. *Carbon*. **2024**, *220*, 118801. DOI: https://doi.org/10.1016/j.carbon.2024.118801
35. He, H.; Zhang, Q.; Wang, H.; Zhang, H. et.al. *J. Power Sources.* **2017**, *354*, 179-188. DOI: https://doi.org/10.1016/j.jpowsour.2017.04.035
36. Zhang, H.; Gao, F.; Zhang, D.; Gao, C.; Huang, G. *Carbon*. **2024**, *230*, 119602. DOI: https://doi.org/10.1016/j.carbon.2024.119602
37. Pandey, V.K.; Verma, S.; Verma, B. *Synth. Met.* **2025**, *311*, 117844. DOI: https://doi.org/10.1016/j.synthmet.2025.117844
38. Wu, H.; Li, L.; Yuan, W. *Chem. Eng. J.* **2022**, *442*, 136259. DOI: https://doi.org/10.1016/j.cej.2022.136259